

FORMULA 1 PERFORMANCE: IN YOUR POCKET

GROUP B4



**ANODISED
ALUMINIUM**

**STRENGTH
RATIO:**
4.7%

STIFFNESS:
1247 N/MM

**CHASSIS
MASS:**
143.5G

MAX TEMP:
35.2 C

**SPECIFIC
STIFFNESS:**
8.7 (N/MM)/G



1 Final Design Overview



Figure 1: Pictures detailing the final chassis design

- **Aluminium chassis mass of 143.5 grams** with optimised dimensions to minimise thermal resistance.
- **Strength ratio of 4.7%** calculated using a maximum von Mises stress of 12.99 MPa from the structural case A: Simple Bending.
- **Stiffness of 1,247 N/mm** calculated using a maximum displacement of 0.0802 mm from the structural case A: Simple Bending
- **Specific stiffness of 8.7 (N/mm)/g**
- **Maximum temperature of 35.2°C** achieved with a combination of graphene layers, anodised aluminium finish with an emissivity of 0.9 and ventilation perforations.
- **Thermal resistance of 4.7 K/W**

2 Introduction

2.1 Problem Statement

In November 2024, 91% of American adults owned a smartphone, up from 35% in 2011, which shows just how quickly mobile technology has become adopted by the general public [1]. However, this rapid increase has not come without design challenges.

Even the most respected of manufacturers have had their faults. With Apple, we saw "Bendgate", where many users complained that their iPhones 6 and 6 Plus were warping in their pockets under relatively low loads[2]. Similarly, with Samsung, we saw that their Galaxy Note 7 was recalled after their attempts to shrink the battery size while increasing capacity which led to short circuits and explosions[3]. These lessons combined with some design constraints help to motivate the Problem Statement provided.

"Design a chassis for a phone which is (1) lightweight and (2) aesthetically attractive yet (3) stiff and strong enough to withstand predefined bending and torsion loads, using a (4) suitable material, and (5) remaining cool despite heat generated by the phone CPU and battery."

2.2 Design Approach

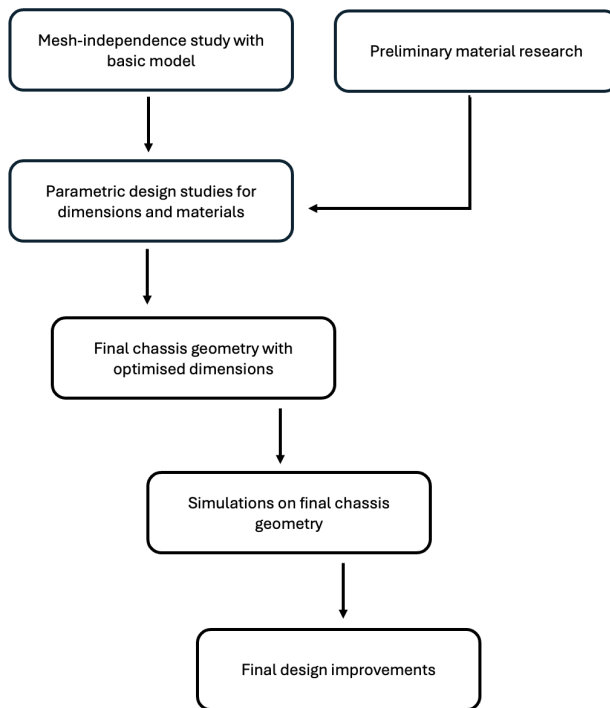


Figure 2: Flow chart for the design approach.

2.3 Group grade scaling factor

Finn O'Connor: 100%: Final CAD modelling, Poster, aesthetics

Robert Dillon: 100%: Editing, mesh refinement, structural simulations

Michael Sadlier: 100%: Introduction, materials, graphene layer, anodised aluminium

Peter Hamilton: 100%: Basic CAD model, Thermal simulations, material research

Magnus Runham: 100%: Material research, mesh refinement, structural simulations

3 Material Research

To determine the most suitable material for the phone chassis, preliminary research was conducted to identify commonly used materials and assess their structural and thermal performance. This reduced our selection to Ti-6Al-4V, 6061-T6, AZ91D and Carbon-Fibre-ThermoPlastic (CFRTP). A side by side comparison of their key properties allowed us to see the trade off between stiffness, weight, and heat conduction which are essential to achieving the optimal chassis design. In addition to mechanical and thermal properties, practical qualities such as cost and real world applicability were also considered.

Table 1: Comparison of Candidate Materials for the Phone Chassis.[4, 5, 6] [7] [8]

Property	Ti-6Al-4V (Titanium)	Al 6061-T6 (Aluminium)	AZ91D (Magnesium)	CFRTP (Carbon Fibre)
Density, ρ (kg/m^3)	4430	2700	1810	1650
Young's Modulus, E (GPa)	113.8	68.9	44.8	24
Tensile Strength (MPa)	950	310	230	440
Yield Strength (MPa)	880	276	150	400
Thermal Conductivity ($\text{W}/\text{m}\cdot\text{K}$)	6.7	167	72.7	8
Specific Stiffness, E/ρ ($\text{GPa}\cdot\text{cm}^3/\text{g}$)	25.7	25.5	24.8	15

From the Table 1, the trade off between different properties are clear. Titanium has the highest strength and elastic modulus, but its high density and poor thermal conductivity make it unsuitable to satisfy our design brief. Similarly, CFRTP has appealing high tensile strength and low density, giving it great mechanical performances while maintaining a low-density structure. Its lightweight and carbon aesthetic make it an attractive candidate for a thin and rigid phone-case chassis. However its weak thermal conductivity effects CFRTP's ability to efficiently dissipate heat. These 2 materials will most likely require additional features in the chassis to aid in heat dissipation. This caused us to focus on Aluminium 6061T6 and Magnesium AZ91D, Magnesium offers a significantly lower density while maintaining competitive stiffness and moderate cooling. Aluminium offers greater stiffness and better thermal conductivity but it has a higher density. Referring back to our design objectives, we chose to focus our study on 2 materials, aluminium and magnesium.

The physical properties show that magnesium is the most suitable material for the phone chassis. As well as its favourable properties, it boasts a high degree of manufacturability due to its low cost, abundance and compatibility with high-precision manufacturing processes. Magnesium's high Specific Stiffness makes it ideal for a lightweight but lasting design, while its metallic finish can support a premium aesthetic through optional coatings or surface treatments. Additionally, magnesium's moderate thermal conductivity allows efficient heat dissipation from the CPU and battery, maintaining user comfort and device reliability [9].

From Table 1 Aluminium 6061-T6 proves to have the most balanced combination of physical properties. The Aluminium alloy offers a unique blend of great mechanical strength, thermal performance and manufacturability. Its high Young's modulus and relatively low density give the material an outstanding stiffness-to-weight ratio. These properties will allow us to manufacture thin, rigid components without sacrificing durability. Aluminium boasts exceptional thermal conductivity (167W/m·K), enabling rapid heat transfer, allowing heat generated by the CPU and battery to be dissipated efficiently throughout the chassis. Aluminium 6061-T6 is corrosion resistant and offers great surface finish capabilities. These characteristics support a long product life and offer an aesthetic consistent with modern consumer markets.

4 Mesh-independence Studies

4.1 Reference Geometry and Material

All mesh-independence studies were performed on a simplified phone chassis model representing the nominal mid-point of the specified design tolerances. The overall dimensions were 160 mm \times 70 mm \times 9 mm, corresponding to the mid-values of the dimensions outlined in the design brief (160 ± 5 mm length, 70 ± 5 mm width, 9 ± 1 mm thickness). A full schematic of the simplified chassis can be found in Appendix A. This simplified geometry excluded fillets, cut-outs, and camera openings to isolate the effect of mesh refinement and ensure that results were independent of geometric complexity.

For the mesh-independence studies, a generic linear-elastic material was applied (6061 Aluminium Alloy). This allowed isolation of numerical mesh effects without introducing variations due to material properties. Final material selection was performed later in the design study.

4.2 Boundary Conditions and Loading

This section describes the fixtures, structural and thermal loads applied to the simplified chassis model for each mesh-independence study. The design brief outlines three loading case: structural case A: simple bending; structural case B: torsion and bending and a thermal case.

For the structural case A, to represent simple bending, the reference model was fixed at one end by a fixed geometry fixture along the horizontal bottom edge as seen in Figure 3(a). The edge on the opposite end was fixed in the Y-plane using a reference geometry fixture. A 100 N distributed load was applied to exposed top surfaces of the model, represented by the purple arrows in Figure 3(a).

For the structural case B, to provide a realistic and numerically stable fixture for the torsion analysis, a 10mm external fillet and an 8mm internal fillet was added to one corner of the chassis model. The external fillet was fixed using a fixed geometry fixture as seen in 3(b). The fillets served to smooth the local geometry at the fixed corner and prevent extreme stress concentrations from the applied constraints. Similarly to case A, a distributed load of 100 N was applied.

For the thermal case seen in Figure 3(c), a heat flux of 0.6 W/cm^2 was applied to a 10 mm \times 10 mm area representing the heat generated by a CPU. A heat flux of 0.06 W/cm^2 was applied to a 120 mm \times 41 mm area to represent the heat generated from a battery. The brief details that a convection coefficient of $10 \text{ W/m}^2\text{K}$ should be applied to all external surfaces. This was interpreted as all surfaces on the outside of the chassis, an is represented in Figure 3(c) by the green indicators.

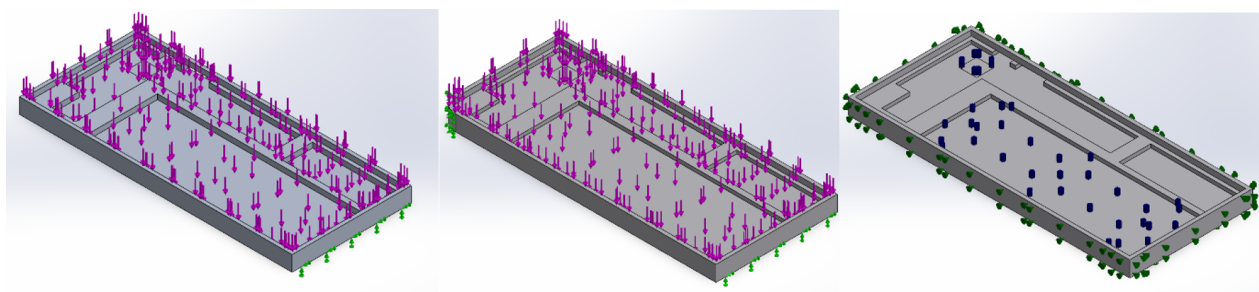


Figure 3: (a) Model setup for case A. (b) Model setup for case B. (c) Model setup for the thermal case.

To establish mesh independence, a convergence criterion was defined whereby the variation of the relative error of the convergence metric between three successive mesh refinements had to be less than 1%. The mesh for each loading case was refined atleast three times with element sizes being halved for each subsequent iteration to determine if the convergence metrics are converging to realistic values.

4.3 Structural Analysis Case A: Simple Bending

The simple bending case was analysed to confirm correct model behaviour and determine an appropriate mesh for the final chassis design case A simulation. As the design brief required the strength ratio of the final model to be based on accurately resolved maximum von Mises stresses, the stress results were required to be independent of the mesh. An initial approach manually refined the global element size incrementally from 8 to 0.5 mm and the corresponding maximum displacement, maximum stress and total strain energy values were recorded. As shown in Table 2, both the displacement and total strain energy responses stabilised with refinement, but the maximum stress started to diverge when the global elements size was reduced to 1 mm evident from the 3.1% relative error from the previous mesh. The final refinement confirms that the maximum stress will not converge to a realistic value recording a 48.6% change from the iteration before.

Table 2: Data from manual stepwise mesh refinement of global mesh size with standard meshing

Manual stepwise mesh refinement	Global mesh element size	Number of elements N_e	Max displacement		Max stress		Equivalent strain energy	
			Value	Rel. error	Value	Rel. error	Value	Rel. error
Too coarse	8	1,937	0.08502	N/A	14.34	N/A	2.653E-03	0.99%
Coarse	4	8,249	0.08544	0.49%	14.36	0.14%	2.667E-03	0.50%
Standard	2	43,261	0.08562	0.21%	14.37	0.07%	2.674E-03	0.26%
Fine	1	334,637	0.08574	0.14%	14.83	3.10%	2.679E-03	0.19%
Very fine	0.5	2,452,557	0.08581	0.08%	28.86	48.61%	2.681E-03	0.1%

This strategy for determining a suitable mesh for the final model simulations was deemed unsuitable as it resulted in unrealistically high stress concentrations that do not represent the true structural behaviour. Accurate maximum stress values are required to calculate the chassis strength ratio, and these values would lead to misleading results. As the mesh was refined, the stresses continued to increase without stabilising, indicating that the mesh was resolving numerical singularities rather than physical stresses. This behaviour is commonly observed at fixed geometry, where sharp corners and fully constrained nodes produce non-physical stress concentrations. Figure 4 illustrates this effect, showing the build-up of stress along the fixed edge. Consequently, this refinement approach was not considered appropriate for assessing realistic maximum von Mises stress values.

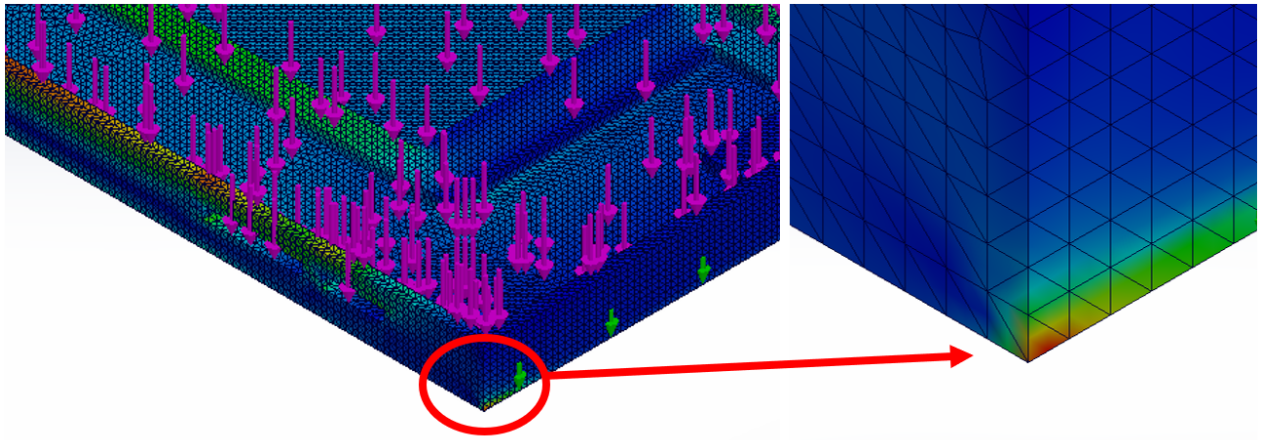


Figure 4: Unrealistic stress concentrations building up along the fixture as the mesh is refined

To mitigate the stress concentrations along the fixture and resolve the stresses where it should reach a maximum in theory, a local mesh control was created along each side of the chassis frame using a 120

mm long Split Line. The location and dimensions of the surfaces created by the Split Line can be seen in more detail in Appendix A. This approach allowed the mesh to be refined in the mesh control region, leaving the unrealistic stress concentrations along the fixtures unresolved. The global mesh element size was kept constant (4 mm) while the mesh control was refined incrementally from 1.6 to 0.2 mm, halving with each subsequent iteration. As shown in Table 3 all three results of interest converged with refinement.

Table 3: Data from manual stepwise mesh control refinement using constant global element size (4 mm)

Manual stepwise mesh refinement	Control mesh element size	Number of elements N_e	Max displacement		Max stress		Equivalent strain energy	
			Value	Rel. error	Value	Rel. error	Value	Rel. error
Standard	1.6	9,574	0.08544	N/A	14.36	N/A	2.667E-03	N/A
Fine	0.8	15,693	0.08544	0.00%	14.36	0.00%	2.667E-03	0.00%
Very Fine	0.4	45,186	0.08546	0.02%	14.36	0.00%	2.668E-03	0.03%
Very Very Fine	0.2	158,558	0.08546	0.00%	14.36	0.00%	2.668E-04	0.00%

Similarly to the first meshing approach, the max displacement and total strain energy values stabilise to values of ≈ 0.085 mm and $\approx 2.67\text{E-}03$ J respectively, nearly identical to the initial study. However, with the mesh control strategy, the maximum von Mises stress stabilises with refinement to a value ≈ 14.36 MPa suggesting that the results are independent of the mesh. Figure 5 shows the stress plot for a mesh with a global element size of 4 mm and a mesh control element size of 0.8 mm. The stresses on chassis are where they should be in theory, concentrated along the frame. The mesh setting shown in Figure 5 will be adopted for the final chassis design simulations.

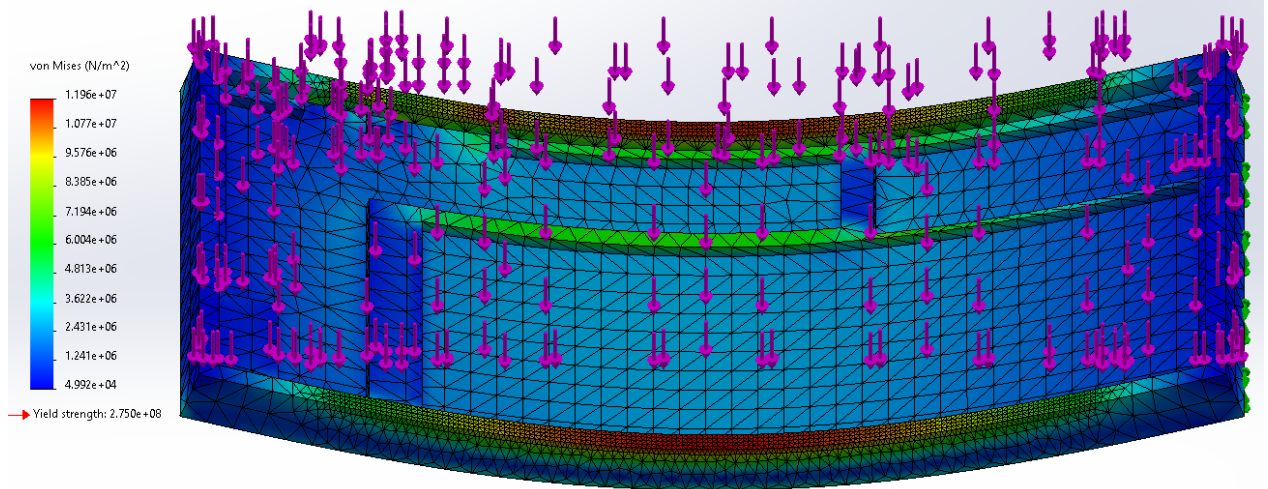


Figure 5: Displacement plot for 4 mm global mesh element size with 0.8mm mesh control element size

4.4 Structural Analysis Case B: Torsion and Bending

For case B, h-adaptive mesh refinement with 98% accuracy and 5 iterations was used with curvature-based meshing enabled starting at 4 mm global mesh element size. The same process was repeated for three starting global mesh element sizes halving for each subsequent simulation as shown in Table 4.

The h-adaptive refinement reduced the total relative strain energy norm error from 11.0% for a starting global element size of 4 mm to 2.13% for a starting global element size of 0.5 mm. This is within 0.13 percentage points off the 2% target set in the study and indicates that the solution is effectively mesh-independent. Further refinement would yield only marginal improvement at significantly higher computational cost.

Correspondingly, as seen in Table 4, the total strain energy stabilised to a value $\approx 1.495\text{E-}03$ J, with changes below 1% between each subsequent starting global mesh element size, satisfying our convergence criteria stated previously. This confirms that further refinement would not significantly alter the results.

For this case, no meshing strategy was found that could accurately resolve the maximum von Mises stresses, as unrealistic stress concentrations developed around the fixed corner of the model. As shown in Table 4, the maximum stress increased from approximately 125 MPa for the coarse mesh to around 2900 MPa for the very fine mesh. This substantial rise in maximum stress values with successive refinements indicates that the results do not stabilise with mesh density, and the stresses observed near the constraint are due to singularities rather than representing a physically meaningful response.

Table 4: Data from h-adaptive mesh refinement study for torsion case

H-adaptive mesh refinement	Global mesh element size	Number of elements N_e	Max displacement		Max stress		Total strain energy	
			Value	Rel. error	Value	Rel. error	Value	Rel. error
Coarse	4	22,328	0.0634	N/A	125	N/A	1.479E-03	N/A
Standard	2	88,704	0.0640	0.98%	328	61.97%	1.489E-03	0.77%
Fine	1	320,064	0.0643	0.47%	782	58.01%	1.495E-03	0.41%
Very Fine	0.5	904,695	0.0645	0.28%	2900	73.03%	1.499E-03	0.24%

Despite the unrealistic stresses at the fixed corner, the displacement and total strain energy values remain stable across all mesh densities, suggesting that the chassis stiffness and deformation were accurately captured. Therefore, the chosen mesh shown in Figure 6 can still be considered appropriate for the final chassis simulations, provided that unrealistic stresses in the fixed regions are excluded from the strength ratio calculations.

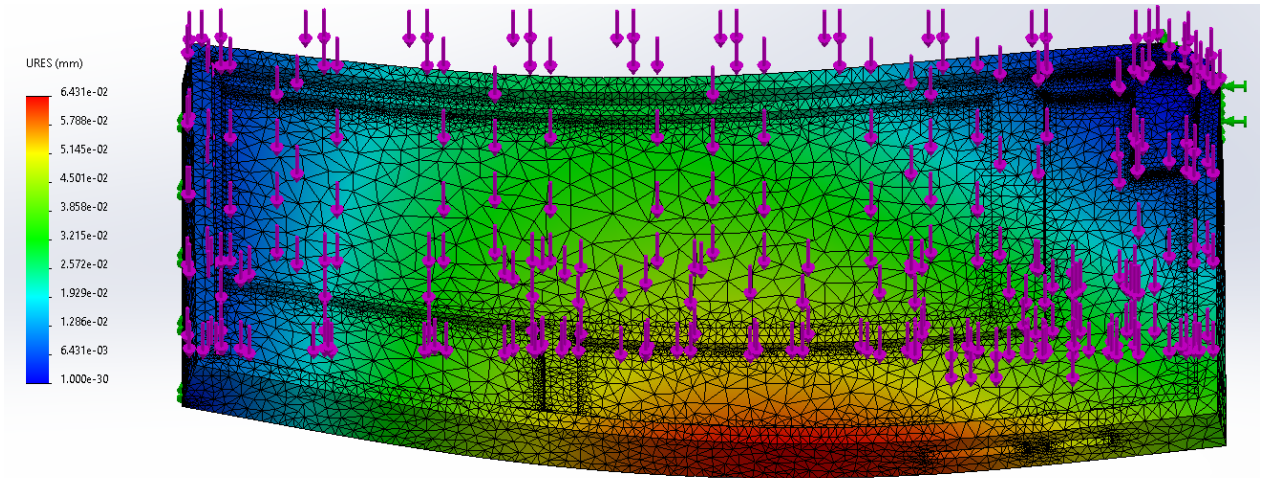


Figure 6: Displacement plot for a 1mm global mesh element size with h-adaptive mesh, 98% accuracy, 5 iterations

4.5 Thermal Analysis

The thermal mesh refinement study was conducted using a manual stepwise approach, reducing the global element size incrementally from 4 to 0.5 mm to assess convergence of the predicted maximum temperature. As shown in Table 5, decreasing the global element size from 4 mm to 1 mm resulted in a significant increase in the total element count, from 8,249 to 334,637 elements. However, the predicted maximum temperature

remained constant at 43.5 °C across all mesh densities, with a relative error of 0.00% between the standard and fine meshes. This indicates that the thermal results are effectively mesh-independent, and that even the standard mesh provides sufficient resolution to capture the temperature distribution accurately.

Table 5: H-adaptive mesh refinement convergence.

Manual Stepwise Mesh Refinement	Global mesh element size	Number of elements N_e	Max temperature	
			Value	Rel. error
Too Coarse	4	8,249	43.5	N/A
Standard	2	43,621	43.5	0.00%
Fine	1	334,637	43.5	0.00%

Consequently, the standard mesh of element size 2 mm, shown in Figure 7 was selected for the final chassis thermal analysis, as further refinement did not yield an improvement in accuracy but substantially increased computational cost.

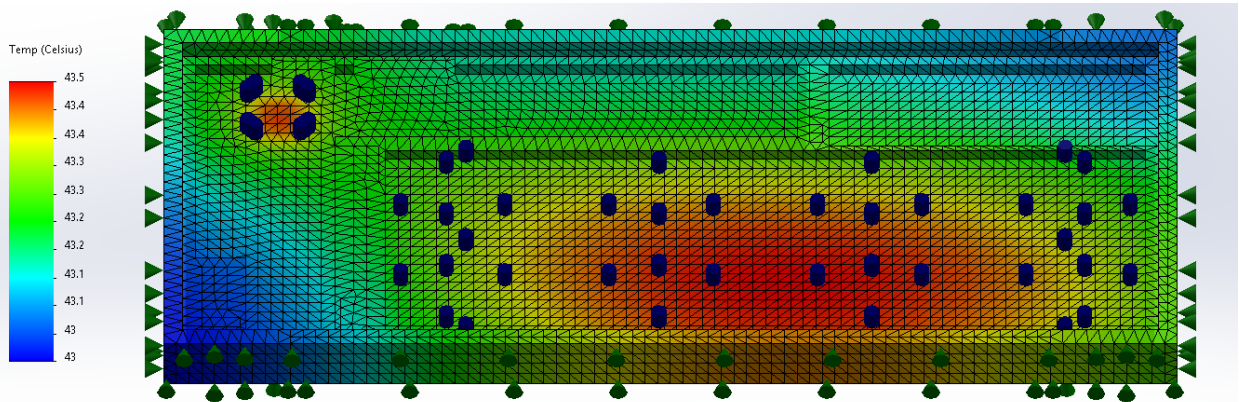


Figure 7: Temperature plot with 2mm global standard mesh element size

4.6 Summary

Summarised in Table 6, three mesh-independence studies were performed to ensure that the simulation results were independent of the mesh. The global element size was reduced incrementally and convergence was assessed based on the variation of the convergence metrics between successive refinements. A deviation threshold of less than 1% for three subsequent iterations was used to define mesh independence, with each iteration halving the previous element size. The selected mesh was therefore confirmed to provide accurate and stable results, suitable for use in the final chassis simulations.

Table 6: Summary of mesh-independence studies: convergence metric; relative error from previous iteration; and selected mesh for final chassis simulations

Case	Convergence metric	Relative error	Selected mesh element size
Simple Bending	Max von Mises stress	0%	Standard, 4 mm global, 0.8 mm mesh control
Torsion and Bending	Total Strain Energy	0.47%	H-adaptive, curvature-based, 2 mm global
Thermal	Temperature	0%	Standard, 2 mm global

Figure 8 displays graphs plotted using MATLAB of the convergence behaviour for all three simulation cases showing the variation of results with decreasing global element size. For both cases A and B, the displacement and total strain energy values stabilised as the mesh was refined, with changes of less than 1% observed between the final three mesh densities, confirming that the models had reached mesh independence. The thermal analysis shows complete convergence even at the standard mesh size, with identical maximum temperature values recorded across all refinement levels. These trends collectively demonstrate that the adopted meshing strategies provide sufficiently accurate and stable results, validating the selected meshes for use in the final chassis simulations.

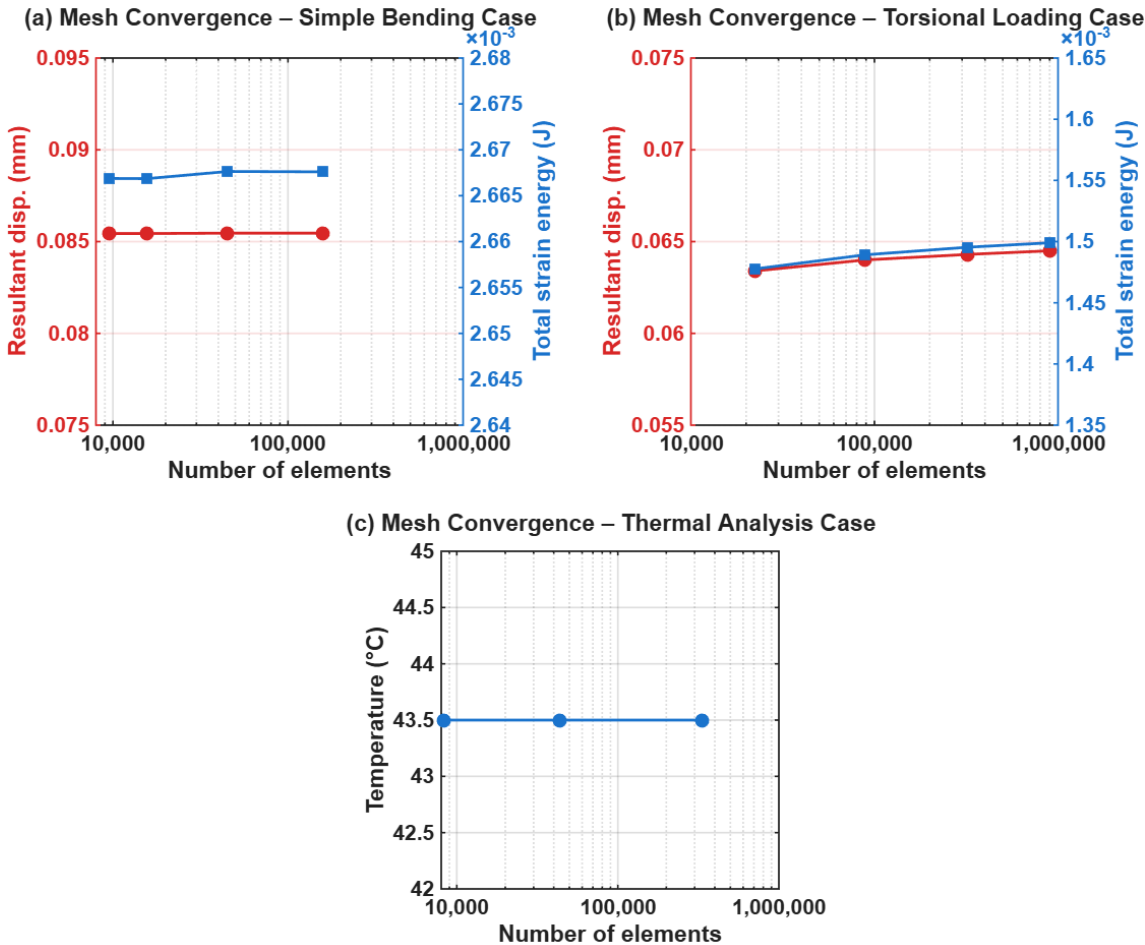


Figure 8: (a) Convergence of displacement and total strain energy values for case A as the number of elements increase. (b) Convergence of displacement and total strain energy values for case B as the number of elements increase. (c) Convergence of temperature for the thermal case as the number of elements increase.

5 Parametric Design Studies

5.1 Dimensional Optimisation

The basic chassis model, using the meshes determined Section 4, was used in two parametric design studies to optimise the geometry and material selection. The objective was to minimise the thermal resistance (R_{th}), the strength ratio, $(\sigma_{vM,max}/\sigma_y)$, and the mass of the chassis, while maximising stiffness, $k = F/\delta$. Thermal resistance, $R_{th} = (T_{max} - T_{amb})/Q_{tot}$, represents the temperature rise per unit of heat generated and is determined from the maximum and ambient temperatures and the total heat load from the CPU and battery.

For this design, the ambient temperature T_{amb} is 20°C as defined in the brief, and the total heat generation Q_{tot} is approximately 3.55 W. Lower R_{th} values indicate improved heat dissipation through the chassis.

The strength ratio was used to assess material utilisation under load. Values below 100% indicate purely elastic behaviour, while a percentage approaching or exceeding 100% suggest yielding or potential structural failure. This metric was used to compare how different materials and geometries influenced load-bearing efficiency without exceeding the yield limit.

A series of simulations were performed in the initial design study which dimensional parameters of the chassis were varied within the limits stated in Table 7. The tolerances are smaller than those stated in the brief, as spaces for PCBs limit the dimensions to the ones shown. The objective was to identify an optimal dimensions that minimised both the temperature and mass while maintaining acceptable mechanical performance in terms of stress and displacement which are reflected in the constraints.

Table 7: Summary of design study variables, constraints, and goals.

Category	Parameter	Description
Variables	Chassis height (mm)	Varied between 156mm and 165mm.
	Chassis width (mm)	Varied between 70mm and 75mm.
	Chassis depth (mm)	Varied between 8mm and 9mm
	Frame thickness (mm)	Varied between 1mm and 3mm
Constraints	Max stress (σ_{max})	≤ 0.6 of yield strength.
	Max displacement	$\leq 1.6\text{mm}$, 1% of reference model height
Goals	Max temperature (T_{max})	Minimise
	Mass	Minimise

The initial design study identified the dimensions 164.8 mm x 75 mm x 9 mm with a frame thickness of 2.95 mm as optimal dimensions. Using these values, the final chassis design was drafted with aesthetic considerations such as adding fillets to the corners and edges. Camera and sensor holes were added as required in the brief, shown in Figure 9. A full schematic of the final chassis design with optimised dimensions can be found in Appendix A.

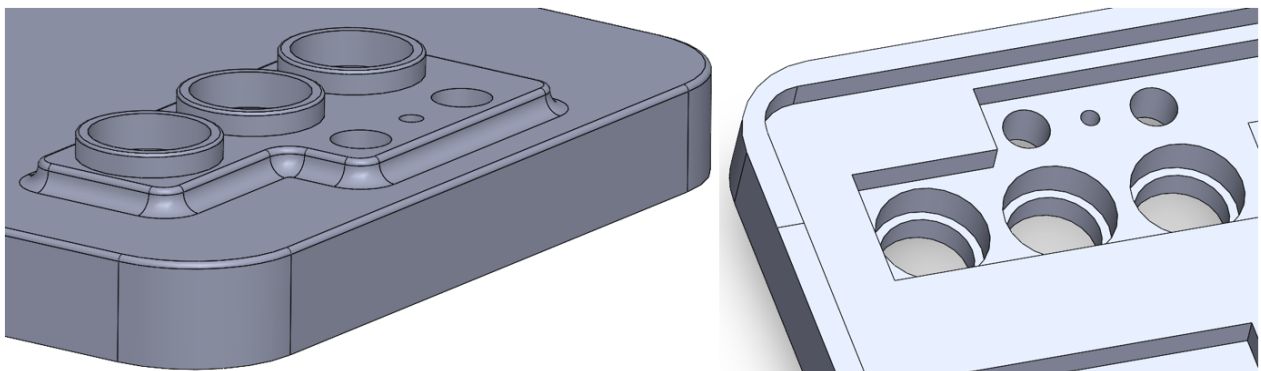


Figure 9: Close up of camera design

5.2 Material Optimisation

The second design study focused on optimising the chassis material to achieve a balance between thermal, structural, and weight. Comparative simulation results for aluminium and magnesium chassis are presented in Table 8. Both materials show similar stress and thermal responses, with maximum von Mises stresses of 13.3 MPa and maximum temperatures of just over 40°C. However, noticeable differences were observed in deformation and mass, with the magnesium chassis showing greater bending and torsion displacements and a lower mass.

Table 8: Comparison of simulation results for aluminium and magnesium chassis designs.

Material	Al 6061-T6 (Aluminium)	AZ91D (Magnesium)
Max von Mises stress (MPa)	13.3	13.3
Simple bending displacement (mm)	0.0807	0.1238
Torsional deformation (mm)	0.0761	0.1173
Max temperature (°C)	40.1	40.6
Mass (g)	143.5	96.2

To further assess the overall performance of each material, mechanical and thermal metrics were evaluated and summarised in Table 10. The aluminium chassis demonstrated higher stiffness (1,239 N/mm) and slightly lower thermal resistance (5.66 K/W) compared to the magnesium design (808 N/mm and 5.80 K/W, respectively). When normalised by mass, the specific stiffness and thermal resistance of the two materials were comparable, although the strength ratio for magnesium was higher, indicating that it operated closer to its yield limit under equivalent loading.

Table 9: Comparison of aluminium and magnesium chassis properties.

Material	Al 6061-T6 (Aluminium)	AZ91D (Magnesium)
Stiffness (N/mm)	1,239	808
Specific stiffness ((N/mm)/g)	8.64	8.39
Strength ratio (%)	4.82	8.87
Thermal resistance (K/W)	5.66	5.80

Although the results were comparable and the magnesium chassis had a lower mass, **Aluminium 6061-T6** was selected for the final design as it has the potential to be anodised to improve both surface durability and thermal performance. The optimised chassis dimensions (see Appendix A) and Aluminium 6061-T6 will therefore be used for final simulations and studies.

6 Simulations and Results

6.1 Structural Analysis Case A: Simple Bending

The final simple bending simulation used the mesh selected from the earlier refinement study, providing reliable and consistent results for the final chassis analysis. The maximum deflection was 0.0802 mm, occurring at the centre of the chassis beam as expected for a simple bending case shown in Figure 10. The deformation shape followed a smooth curvature consistent with beam theory, confirming correct loading and constraint conditions. The deflection magnitude represents less than 0.05% of the chassis height, indicating high stiffness and minimal deformation under normal use.

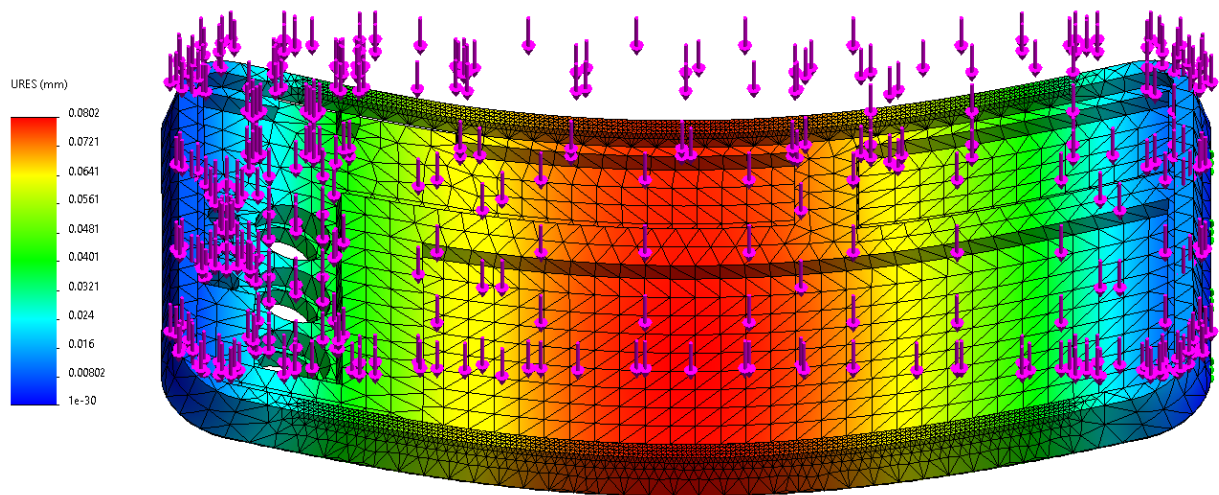


Figure 10: Resultant displacement plot for structural case A: simple bending.

The von Mises stress distribution shown in 11 showed a maximum of 12.99 MPa along the chassis frame as expected. The result is significantly below the 276 MPa yield strength of Aluminium 6061-T6. This confirms the structure remains entirely elastic. The stress distribution is smooth and symmetrical, further indicating correct boundary definition and that there are no unrealistic stress concentrations along the fixed geometry.

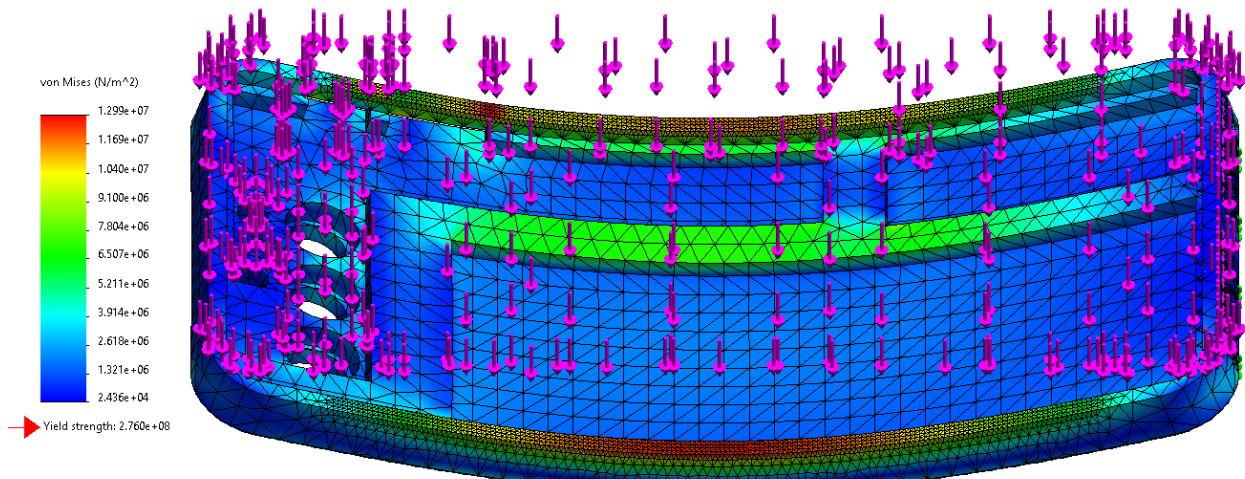


Figure 11: Von Mises stress plot for structural case A: simple bending.

Using the applied load of 100 N and the measured maximum displacement from the simple bending case, the bending stiffness of the chassis works out to $\approx 1,247$ N/mm, which is in line with the earlier results for the basic and confirms the structure is relatively stiff for its size. Taking the aluminium chassis mass of 143.5 g, this gives a specific stiffness of roughly 8.7 (N/mm)/g, showing that the design provides good rigidity without excessive weight. The maximum von Mises stress from the same simulation was 12.99 MPa, and comparing this to the aluminium yield strength of 276 MPa gives a strength ratio of about 4.7%, meaning the chassis is operating very comfortably within the elastic range and has a large safety margin. Together, these results show that the selected mesh and geometry not only capture the bending behaviour correctly but also that the design is stiff, light, and far from yielding. A brief buckling simulation gave a buckling FoS ≈ 400 , confirming that buckling is also not a concern. These results suggest the chassis is structurally efficient and conservative. In future designs, there may be potential to reduce frame thickness or optimise geometry further to reduce the mass.

6.2 Structural Analysis Case B: Torsion and Bending

For case B, the same mesh selected in the earlier mesh-independence study was used, so the results are directly comparable to the simple bending case. The displacement plot shown in Figure 12 shows a smooth and physically realistic deformation pattern, with the maximum displacement occurring close to where expected, at the free corner, which confirms that the boundary conditions and load application are correct.

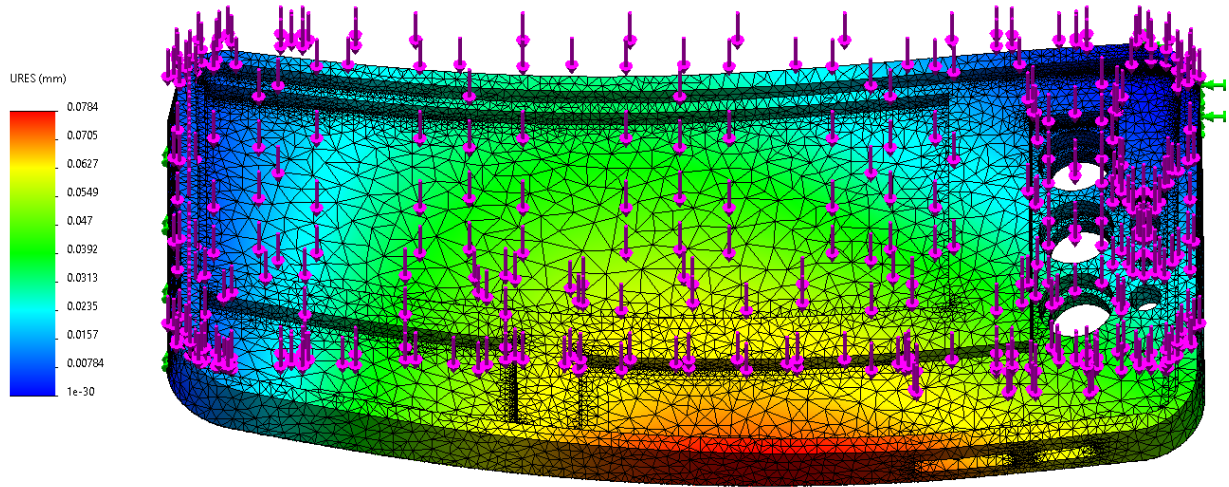


Figure 12: Resultant displacement plot for the structural case B: torsion and bending.

Using the applied load of 100 N and the recorded maximum displacement of 0.0784 mm gives a stiffness of $\approx 1,275$ N/mm, and with the same chassis mass of 143.5 g this corresponds to a specific stiffness of ≈ 8.9 (N/mm)/g. This is very close to, but not exactly the same as, the value obtained from the pure bending case; because the simple bending load case is more controlled and better aligned with beam theory, that earlier stiffness value is taken as the more representative value for the chassis. Unlike the displacement, the von Mises stresses from case B could not be used to calculate a strength ratio, because the mesh refinement study showed that stresses near the fixed corner did not converge and continued to rise with refinement, so the maximum stress values are considered non-physical and are excluded from the analysis.

Because the torsion case was the most mesh-sensitive of the load cases, an additional h-adaptive convergence study was run for the final chassis model to show that, even though local von Mises stresses near the constraint did not stabilise, the overall solution was still converging. Starting from the 2 mm global element size selected in the earlier refinement study, the h-adaptive solver refined the model over five iterations and reached a reported global criterion of total relative strain energy norm error below about 4.5%, which was

2.5% off the target accuracy of 98%. The convergence plot shown in Figure 13 for this case shows exactly what is expected: the normalised total relative strain error stabilises in the first few refinements, and the target-accuracy curve flattens out toward the fifth iterations. This supports using the selected mesh for case B and suggests the displacement results are accurate.

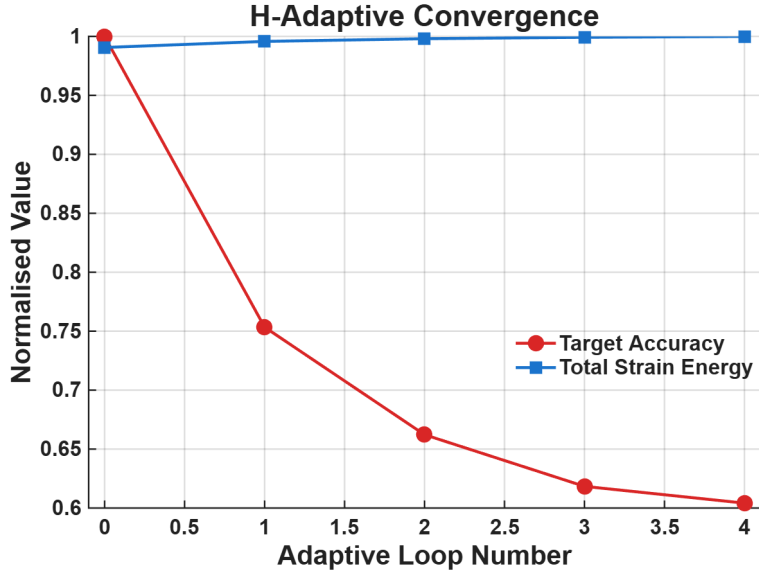


Figure 13: H-adaptive convergence graph for case B starting from 2 mm global mesh element size with a target accuracy of 98% over 5 iterations.

6.3 Thermal Analysis

The initial thermal study shown in Figure 14 shows a maximum temperature of 40.1°C and a minimum of 39.3°C under the applied CPU and battery heat load. This small temperature difference indicates good internal heat spreading, but the overall temperature level suggests limited heat dissipation to the surroundings. These results provide a useful baseline, and future design iterations will aim to lower the maximum temperature.

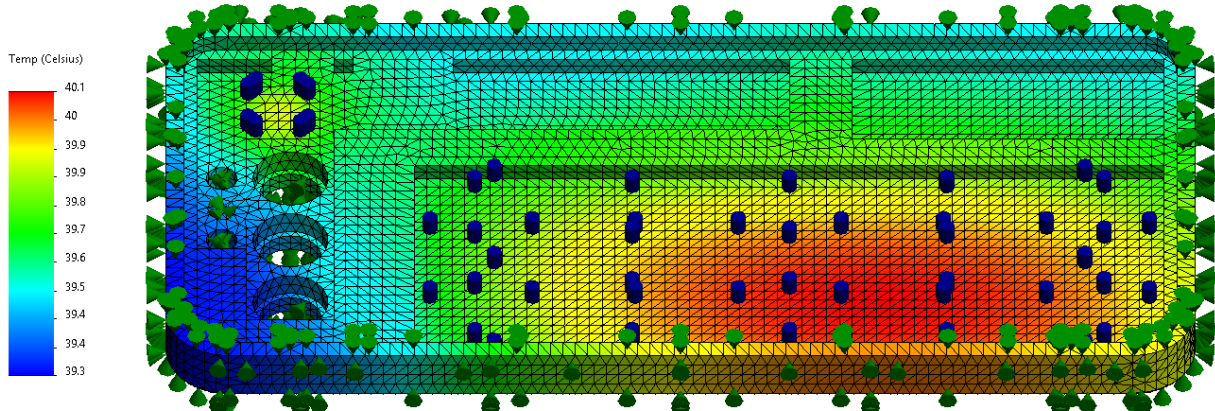


Figure 14: Temperature plot for the thermal case with the final chassis model

Grooves or other surface features were not considered in the chassis design, as these would disrupt the clean external appearance. While these features could improve heat dissipation by increasing surface area, they would detract from the intended aesthetic so other strategies for getting heat out of the chassis were explored.

6.3.1 Graphene Layer

Graphene is a one-atom thick sheet of carbon whose atoms are arranged in a hexagonal (honeycomb) lattice. Each carbon forms three sp^2 bonds that create a stiff, well connected network. Heat-carrying phonons are able to travel rapidly in-plane, which gives graphene a very high in-plane thermal conductivity of up to 4000 W/m·K[10]. When sheets are stacked, to create graphite, weak Van der Waals forces between each of the layers inhibit heat flow and can drop cross-plane conductivity to around 10 W/m·K. As a result, graphene is an ideal material for 2D heat dissipation [11]. For the SolidWorks simulations, a graphene plate which is a compressed multi-layer graphene film, will be used. This will retain high in-plane thermal conductivity for heat spreading across its surface, taking an in-plane thermal conductivity of 1400 W/m·K as specified in the product description [12].

Due to the fact that graphene plates are electrically conductive, great care must be used with regards to how it is used next to the conductive aluminium chassis. The most effective layering from the battery to the chassis would be: **Battery → Dielectric Layer → Graphene Plate → Insulating Thermal Interface Material (TIM) → Aluminium Chassis**. This layout would keep the battery electrically isolated while still letting the graphene spread heat and the TIM transfer that heat into the chassis efficiently.

For the simulations, the graphene plate will be modelled as bonded to the chassis. This replicates the use of a TIM and is sufficient for the thermal and structural simulations. The dielectric will also be omitted in the CAD model, as it will have a negligible effect on thermal performance and stiffness.

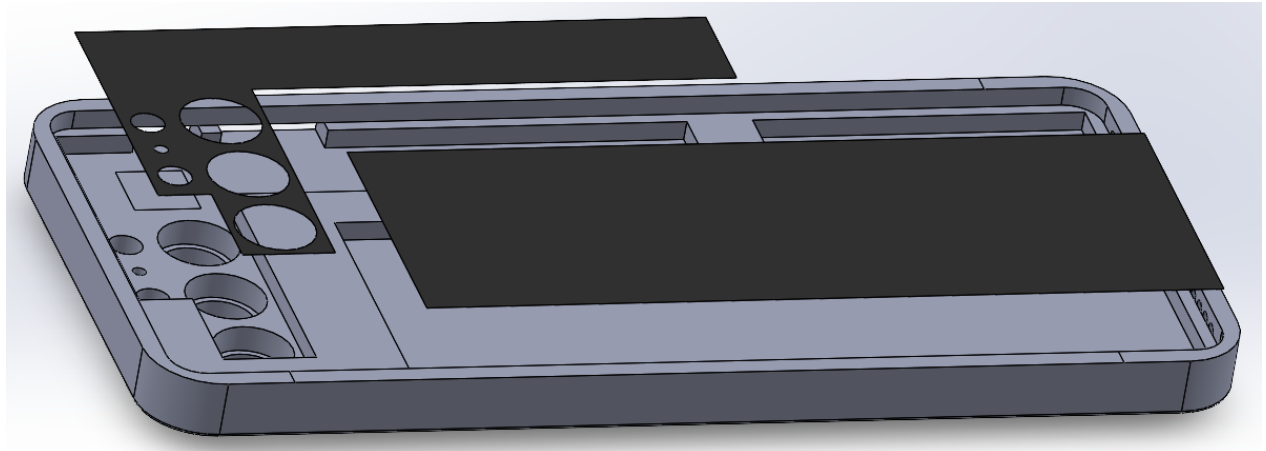


Figure 15: Exploded view showcasing the chassis model with graphene layers

Using the same simulation set up as the initial thermal study, adding the thin graphene layer beneath the CPU and battery slightly improved heat spreading, reducing the temperature range to 39.8 to 39.1°C. The change was minimal, indicating that thermal performance is limited more by overall chassis conduction than heat dissipation within the chassis.

6.3.2 Anodised Finish

The outer surface of the aluminium chassis will be anodised to replace the soft metallic skin with a thin aluminium-oxide layer that is mechanically harder and more wear resistant than bare 6061-T6. This improves the chassis' aesthetics and gives it a stable finish without needing to use paints that can wear over time and begin to peel. [13]

Not only will an anodised exterior enhance the chassis' aesthetics and wear resistance but will similarly greatly improve its thermal properties. Bare aluminium radiates heat poorly due to its low emissivity, whereas anodised finishes, especially black finishes, can reach emissivities greater than 0.9 which greatly improves

the chassis ability to remove passive heat from its surface, increasing longevity and improving touch comfort [14]. The effects of an anodised finish was simulated by added a radiation load to the external surfaces of the chassis as shown in Figure 16 and setting the emissivity to 0.9 and an ambient temperature of 293.15 K.

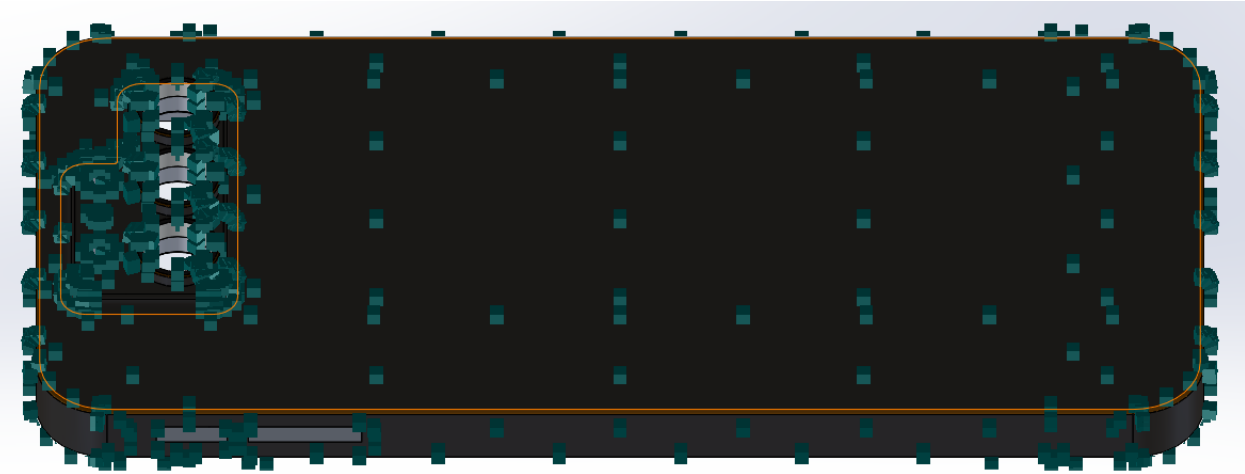


Figure 16: Simulation set up using a radiation load to represent a high emissivity anodised finish.

This produced a significant improvement, reducing the maximum temperature to 35.5°C and the minimum to 34.8°C. The anodised coating improves surface heat emission, while the graphene improves local heat spreading, together providing a noticeable reduction in overall operating temperature.

6.3.3 Vent Perforations

Small perforations shown in Figure 17 were added along the lower edge of the chassis to increase surface area and to increase convective heat transfer. These surfaces were considered external surfaces so the convection and radiation loads were applied to the perforations in the next thermal simulation.

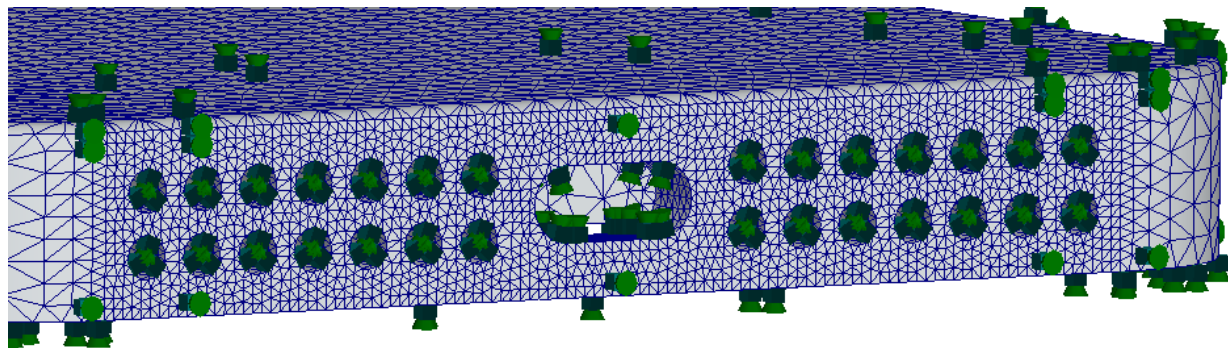


Figure 17: Caption

When combined with the anodised surface finish and graphene layers, the addition of small perforations along the lower edge of the chassis produced the most effective overall thermal performance, reducing the operating temperature range to 35.2 to 34.8°C as shown in Figure 18. This represents the lowest and most uniform temperature distribution achieved across all tested designs. The improvement confirms that even subtle design changes which promote airflow, when integrated with better surface emissivity can significantly improve thermal performance without compromising the chassis appearance. The final design therefore combines these three features: anodised aluminium; graphene layers, and discrete perforations

as the finalised design for the chassis. The resulting maximum temperature of 35.2 °C is well within safe operating limits

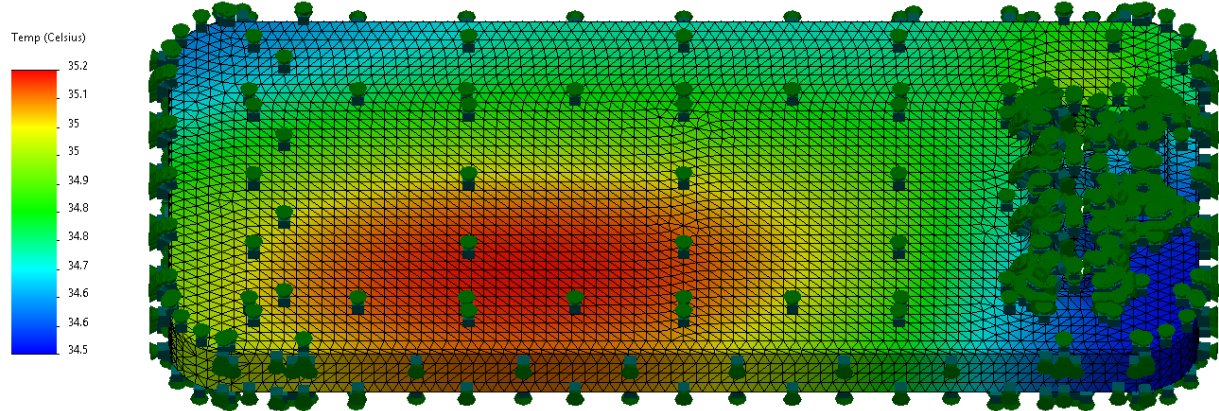


Figure 18: Temperature plot for thermal analysis of final chassis design

Using the total heat generation of 3.55 W, a maximum temperature of 35.2°C, and an ambient temperature of 20°C, the overall thermal resistance for the final design is $\approx 4.3 \text{ K/W}$. This shows a clear improvement over earlier designs and confirms that the combination of anodisation, graphene layers, and small ventilation perforations provides sufficient heat transfer while maintaining the chassis aesthetic.

7 Summary

The simulation results demonstrated that the final chassis design meets acceptable standards in structural and thermal performance. Under bending and torsional loading, the chassis showed very low deflections and stresses well under the yield strength, confirming a high level of stiffness and a wide safety margin against failure or buckling. Thermal studies showed progressive improvements through each design stage, with the combination of anodised aluminium, graphene layers, and small ventilation perforations producing the best overall performance. The final chassis properties are summarised in Table

Table 10: Summary of final aluminium chassis properties.

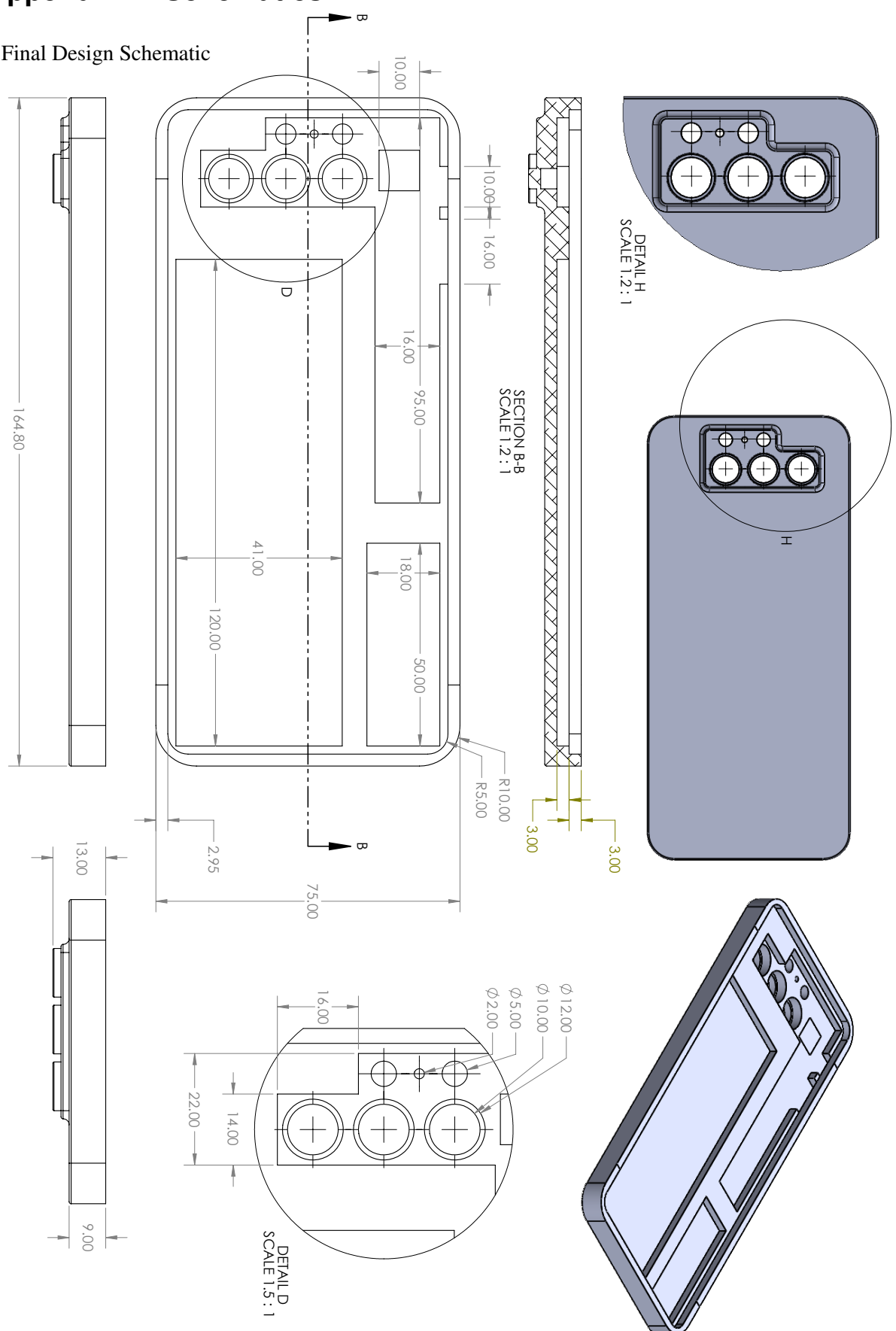
Material	Al 6061-T6 anodised aluminium
Stiffness (N/mm)	1,247
Specific stiffness ((N/mm)/g)	8.7
Strength ratio (%)	4.7
Thermal resistance (K/W)	4.3
Mass (g)	143.5

References

- [1] “Demographics of Mobile Device Ownership and Adoption in the United States.” [Online]. Available: <https://www.pewresearch.org/internet/fact-sheet/mobile/>
- [2] Ziah and J. Jia, “Impact of Firm Specific Factors and Macroeconomic Factors toward Unemployment Rate: A Study on Corporate Scandal,” May 2019.
- [3] “Benefits and Costs of Closed Innovation Strategy: Analysis of Samsung’s Galaxy Note 7 Explosion and Withdrawal Scandal.” [Online]. Available: <https://www.mdpi.com/2199-8531/4/3/20>
- [4] “ASM Material Data Sheet - Titanium Ti-6Al-4V.” [Online]. Available: <https://asm.matweb.com/search/specificmaterial.asp?bassnum=mtp641>
- [5] “ASM Material Data Sheet - Aluminum 6061-T6.” [Online]. Available: <https://asm.matweb.com/search/specificmaterial.asp?bassnum=ma6061t6>
- [6] “Magnesium AZ91D-F, Cast.” [Online]. Available: <https://www.matweb.com/search/datasheet.aspx?MatGUID=07baafbb9c364fb18fd413bceced867f&ckck=1>
- [7] J. Shi, M. Mizuno, L. Bao, and C. Zhu, “A Facile Molding Method of Continuous Fiber-Reinforced Thermoplastic Composites and Its Mechanical Property,” *Polymers*, vol. 14, no. 5, p. 947, Feb. 2022. [Online]. Available: <https://www.mdpi.com/2073-4360/14/5/947>
- [8] L. B.-L. GmbH, “Tepex Dynalite 102-RG600(47%) PA6 Product Datasheet,” LANXESS AG, Cologne, Germany, Tech. Rep. -, 2021. [Online]. Available: <https://tepex.lanxess.com/>
- [9] J. Zhang, J. Miao, N. Balasubramani, D. H. Cho, T. Avey, C.-Y. Chang, and A. A. Luo, “Magnesium research and applications: Past, present and future,” *Journal of Magnesium and Alloys*, vol. 11, no. 11, pp. 3867–3895, Nov. 2023. [Online]. Available: <https://www.sciencedirect.com/science/article/pii/S2213956723002694>
- [10] M. Sang, J. Shin, K. Kim, and K. J. Yu, “Electronic and Thermal Properties of Graphene and Recent Advances in Graphene Based Electronics Applications,” *Nanomaterials*, vol. 9, no. 3, p. 374, Mar. 2019, publisher: Multidisciplinary Digital Publishing Institute. [Online]. Available: <https://www.mdpi.com/2079-4991/9/3/374>
- [11] C. Yu, W. Zeng, Z. Kou, W. Wang, L. Wang, Q. Li, X. Liu, and Z. Dai, “Transparency of Graphene to Solid-Solid van der Waals Interactions,” *Physical Review Letters*, vol. 135, no. 15, p. 156202, Oct. 2025. [Online]. Available: <https://link.aps.org/doi/10.1103/jgqz-gwlc>
- [12] “Graphene Sheet, Size: 1 cm x 1 cm, Thickness: 35 µm, Highly Conductive.” [Online]. Available: <https://shop.nanografi.com/graphene/graphene-sheet-size-1-cm-x-1-cm-thickness-35-m-highly-conductive/>
- [13] J. Cabral-Miramontes, C. Gaona-Tiburcio, F. Estupinán-López, M. Lara-Banda, P. Zambrano-Robledo, D. Nieves-Mendoza, E. Maldonado-Bandala, J. Chacón-Nava, and F. Almeraya-Calderón, “Corrosion Resistance of Hard Coat Anodized AA 6061 in Citric–Sulfuric Solutions,” *Coatings*, vol. 10, no. 6, p. 601, Jun. 2020, publisher: Multidisciplinary Digital Publishing Institute. [Online]. Available: <https://www.mdpi.com/2079-6412/10/6/601>
- [14] Y. Goueffon, L. Arurault, S. Fontorbes, C. Mabru, C. Tonon, and P. Guigue, “Chemical characteristics, mechanical and thermo-optical properties of black anodic films prepared on 7175 aluminium alloy for space applications,” *Materials Chemistry and Physics*, vol. 120, no. 2, pp. 636–642, Apr. 2010. [Online]. Available: <https://www.sciencedirect.com/science/article/pii/S0254058409007627>

Appendix A: Schematics

1. Final Design Schematic



2. Basic Reference Design Schematic

